

RSC Advances



This is an *Accepted Manuscript*, which has been through the Royal Society of Chemistry peer review process and has been accepted for publication.

Accepted Manuscripts are published online shortly after acceptance, before technical editing, formatting and proof reading. Using this free service, authors can make their results available to the community, in citable form, before we publish the edited article. This *Accepted Manuscript* will be replaced by the edited, formatted and paginated article as soon as this is available.

You can find more information about *Accepted Manuscripts* in the [Information for Authors](#).

Please note that technical editing may introduce minor changes to the text and/or graphics, which may alter content. The journal's standard [Terms & Conditions](#) and the [Ethical guidelines](#) still apply. In no event shall the Royal Society of Chemistry be held responsible for any errors or omissions in this *Accepted Manuscript* or any consequences arising from the use of any information it contains.

ARTICLE

Three-dimensional ultrathin Sn/polypyrrole nanosheets network as high performance lithium-ion battery anode

Xin Fan,^a Anni Jiang^a, Peng Dou^a, Daqian Ma^a and Xinhua Xu^{a,b,*}

In order to optimize the electrode system of lithium-ion battery for problems such as lithium ion diffusion, electrons transportation, and large volume changes during cycling processes, a novel anode material composed of ultrafine Sn nanoparticles (~5 nm) anchored inside well-connected three-dimensional (3D) polypyrrole (PPy) nanosheets network has been designed and synthesized through a simple microemulsion-based preparation of tin nanoparticles with organic crystal surface-induced PPy polymerization. In this electrode material, the ultrathin PPy coating (~3-4 nm) plays a “flexible confinement” function to preserve the structural and interfacial stabilization of inner Sn nanoparticles as well as a “binder” function to suppress the detachment of Sn from the collector. Meanwhile, the continuous conductive PPy nanosheets network with open structures and large contact surface for Sn nanoparticles dispersion can provide an easy access and a short path length for Li⁺ intercalation. As a result, the integration of 3D conductive network and ultrafine Sn nanoparticles with ultrathin *in-situ* PPy coating induces improved structural integrity and accessible capacity for Sn nanoparticles electrode. It delivered high capacity retention of 766 mAh g⁻¹ after 200 cycles at the current density of 0.2 A g⁻¹ and a reversible capacity of 583 mAh g⁻¹ when kept at a much higher current density of 2 A g⁻¹.

Introduction

Lithium-ion batteries have been widely used to power portable electronic devices because of the highest energy density among existing rechargeable batteries [1]. Moreover, lighter or smaller design is one of the main trends for their development in order to meet the further requirement of portability. Therefore, a large energy density of electrode material is of great importance. Tin-based materials have been intensively studied as anode materials for lithium-ion batteries not only due to their high theoretical capacity of about 993 mAh g⁻¹, a value that is three times higher than that of graphite [2,3], but also for their high volumetric capacity of about 7254 mAh cm⁻³, which is about nine times as high as graphite (818 mAh cm⁻³) [4]. The volumetric energy density is the most relevant metric for portable lithium-ion batteries applications [4]. However, the drastic volume change of Sn-based electrode would cause severe mechanical damage and lead to rapid capacity fading during cycling.

To address this challenge, major efforts have been centered on the development of novel nanostructures of Sn-based anodes. Among them, core/shell nanostructures have

become a hotspot in the field of lithium-ion batteries, which is expected to exploit ideal matrices to confine the volume change and keep the integrality of anode materials by “cushion effect”. Various designs of Sn based nanocomposites driven by the possibility of combining their high lithium storage properties with enhanced stability have been frequently investigated on account of the matrix’s good environmental stability and high conductivity [5-9]. Typically, judicious combinations of conducting polymers, such as polyaniline [10,11], poly(3, 4-ethylenedioxythiophene) [12], and polypyrrole [13-18], with selected metal or metal oxide with tailored structures as anode materials are fascinating due to their underlying synergistic effect and simple fabrication procedure [19]. They have been explored as core/shell nanostructures and demonstrated to effectively buffer the substantial volume change, and offer electrical conduction pathways to the active materials [15-18], leading to considerably improved cycle stability and a higher reversible specific capacity. Nevertheless, reports about shape control of conductive polymers are limited. The main challenge is to controllably synthesize metal (oxide)/conducting polymer composites with bespoke architectures for developing advanced functional materials with enhanced device performance or new

useful properties.

Generally, in order to increase mass loading of the active materials on the current collectors without sluggish Li^+ intercalation caused by the shortage of active surface exposure [20], 3D designs with open nanostructures have been highly desirable for their enhanced electrochemical properties, such as 3D nanowire/tube arrays [21,22], coaxial nanostructures [23,24], porous foams [25,26], and so forth. The high surface area and high porosity associated with the open nanostructures, shortened ionic pathways and direct connection with the current collector without insulating binders usually translate into high electrochemical capacities and good rate performance for lithium-ion batteries. Nevertheless, it is still urgently needed to explore the corresponding efficient assembly methods for the fabrication of lithium-ion batteries.

Inspired by the aforementioned works, we put forward a facile synthesis of novel anode material composed of ultrafine Sn nanoparticles anchored in a 3D conductive PPy nanosheets network. The PPy network acts as both binder and conductive matrix for the dispersion of Sn nanoparticles. It is capable of forming a conformal coating that binds Sn nanoparticles with the current collector tightly and can serve as a geometrical coating to insure the structural and interfacial stability of tin nanoparticles during cycling. Furthermore, the distinct 3D ultrathin PPy nanosheets network with large surface area can provide a stable support for the high dispersion of Sn nanoparticles as well as the highway for electron/ Li^+ transport. Using the designed 3D Sn/PPy electrode, outstanding electrochemical performance has been achieved, such as stable reversible capacity, high coulomb efficiency, and superior rate capacities upon increased currents, indicating that this simple synthetic strategy can be considered as a promising candidate for practical applications among lithium-ion batteries anodes.

Experimental

All chemicals were of analytical grade and used without further purification. $\text{SnSO}_4 \cdot 2\text{H}_2\text{O}$ (>99%), poly(vinylpyrrolidone) (PVP), sodium borohydride (NaBH_4 , >98%), sodium hydroxide (NaOH , >96%), sodium dodecyl sulfate (SDS), ammonium persulfate (APS) were obtained from Kewei Chemical Reagent Co. Ltd. of Tianjin University (Tianjin, China). Pyrrole monomer (98% reagent grade) and phytic acid (50% w/w in H_2O) were purchased from Sigma-Aldrich PTE. Ltd in Singapore.

2.1. Preparation of tin nanoparticles

Tin nanoparticles were synthesized by a microemulsion-based chemical reduction. The metal precursor microemulsion solution was prepared by adding 0.1 g $\text{SnSO}_4 \cdot 2\text{H}_2\text{O}$, 0.05 g PVP and 0.02 g SDS to 40 ml sulphuric acid solution. The reducing agent solution was prepared by adding 0.2 g NaBH_4 to 40 ml deionized water (DI water), and the pH was adjusted to 12 using 2 M NaOH solution. The reducing agent solution was added drop-wise into the metal precursor solution under strong magnetic stirring. The solution turned brown immediately after adding the reducing agent solution. After completely adding,

the mixed solution was stirred for another 2 hours. Then, Sn nanoparticles were obtained by centrifugation (Xiangyi-H1650-W, supercentrifuge) at 10,000 rpm for 10 min and then washed with distilled water 5 times and ethanol 3 times. After the mass of Sn nanoparticles was measured, the Sn nanoparticles was suspended again and sonicated in ethanol until a homogeneous suspension was achieved. The growth of the Sn nanoparticle is suppressed by the absorption of PVP on the surface of Sn nanoparticles, and the SDS molecules' secondary adsorption on the PVP layer with their negative charged hydrophilic group towards outside greatly avoid the agglomeration between Sn nanoparticles through electrostatic repulsion, thereby resulting in smaller nanoparticles.

2.2. Preparation of 3D Sn/PPy composites and relevant electrodes

The Sn/PPy composite is prepared via a scalable solution phase synthesis. First, the as-prepared ultrafine Sn nanoparticles and 0.1 M SDS were evenly dispersed in DI water under strong magnetic stirring and kept below 0°C . Then 30 μL pyrrole monomer (98% reagent grade, Sigma Aldrich) and 60 μL phytic acid solution (50% w/w in H_2O , Sigma Aldrich) were added in the brown suspension as shown in Fig. S1a. Before polymerization, the monomer was distilled and preserved against exposure to light to prevent residual polymerization. After sufficient stirring for an hour, 600 μL 0.7 M APS aqueous solution was slowly dropped into the above solution. The solution was sonicated for 5 min to form a homogeneous black Sn/PPy product (Fig. S1b) before it was bladed onto a copper foil. Then the polymerization went on for at least 5 minutes on the copper foil. Finally, the product was immersed in DI water for 10 h to completely remove excess inorganic salts in the anode material and then dried under vacuum at room temperature ($\sim 20^\circ\text{C}$). The electrode film was pressed at 10 MPa to achieve better adhesion of the active material to the Cu current collector. The typical electrode material loading was 0.45 mg cm^{-2} . Fig. S1c shows an example of a uniformly coated electrode film (5 cm \times 20 cm). This solution-based synthesis method and its compatibility with roll-to-roll coating methods make this system readily scaled for large area electrode film.

2.3. Preparation of Sn@PPy composites and relevant electrodes

The Sn@PPy composites were prepared using bigger Sn nanoparticles synthesized in our previous work [27]. The Sn nanoparticles with an average diameter of 30-50 nm and 0.1 M SDS were evenly dispersed in deionized water under strong magnetic stirring at room temperature. Then 30 μL pyrrole monomer (98% reagent grade, Sigma Aldrich) was added in the brown suspension. After sufficient stirring for an hour, 600 μL 0.7 M ammonium persulfate aqueous solution was slowly dropped into the above solution. Then the solution was stirred for another 5 h to form a homogeneous black Sn@PPy liquid product. In the end, Sn@PPy nanoparticles were collected by centrifugation and then washed with distilled water 5 times and ethanol 3 times.

The *in-situ* PPy coating Sn nanoparticles electrode and the pristine Sn nanoparticles electrode without any surficial decoration were prepared by coating the slurry made by dissolving the active material powders (Sn@PPy nanoparticles, or Sn nanoparticles, 80 wt.%), acetylene black (10 wt.%) and polyvinylidene fluoride (PVDF) (10 wt.%) in *n*-methyl pyrrolidinone onto Cu foil substrates. Then, the electrodes were pressed at 10 MPa and dried at 90 °C under vacuum for 4 h. The two electrodes using traditional non-conductive PVDF as binder were denoted as Sn@PPy/PVDF and Sn/PVDF, respectively.

2.4. Characterization

The morphology of the as-prepared samples was investigated by a Hitachi S-4800 field-emission scanning electron microscope (FE-SEM) at an accelerating voltage of 5 kV and a high-resolution transmission electron microscope (HR-TEM, JEM-2100F) operated at 200 kV. The composition of the electrode material was investigated using Genesis XM2 energy dispersive X-ray spectroscopy (EDS, USA). The Brunauer-Emmett-Teller (BET) specific surface area analysis was performed by measuring the N₂ adsorption-desorption isotherms at 77 K on a BelSorp-Mini instrument. The crystal structure of the product was characterized by X-ray powder diffraction (XRD) using an automated D/MAX-2500 X-ray diffractometer with monochromatic Cu K α radiation, the 2 theta Bragg angles were scanned over a range of 25-85° at a rate of 5.0° min⁻¹. The vibrational characteristics of the samples were analyzed via Raman spectroscopy (JOBIN-YVON, LABRAM model) using a 632 nm He-Ne laser as the excitation source, in the range of 100-3500 cm⁻¹. Thermogravimetry analysis (TGA, NETZSCH, STA449F3) was measured from 50 to 800 °C at a heating rate of 10 °C min⁻¹ in air, to evaluate the weight content of Sn and PPy in these composites. The morphology of the hydrated C₁₂H₂₅SO₄Na crystals was observed using optical microscopy (OM, Olympus BX-51). The electrode materials after been cycled for 200 times were washed with acetonitrile in the glovebox and then sealed in a hermetic bag before we took them out to test.

Electrochemical performance was investigated directly using coin cells (type CR2032) assembled in an argon-filled glove box. Li metal foil was utilized as the counter electrode, 1 M LiPF₆ in ethylene carbonate (EC) and dimethyl carbonate (DMC) (1:1 by volume) was used as the electrolyte, 3D Sn/PPy composites coated on copper foil was used as the positive electrode and Celgard 2400 was used as the separator. Each cell was aged for 24 h at room temperature before starting the electrochemical tests. The galvanostatic charge/discharge measurements and rate performance were performed over the potential range 0.01-1.5 V (versus Li⁺/Li) using an MTI Battery Testing System at room temperature. The electrochemical impedance spectroscopy (EIS, 0.1~1×10⁶ Hz) and cyclic voltammetry (CV, 3.0-0.0 V) were carried out by a CHI 660D system. All the specific capacities are reported based on the weight of Sn.

Results and discussion

The detailed structure of 3D Sn/PPy composite is schematically illustrated by FE-SEM. Evidently, the SEM image in Fig. 1a indicates that the 3D network structure of pure PPy matrix is consisted of interconnected PPy nanosheets with uniform thicknesses of about 7-10 nm. It is conspicuous to observe the edges of individual sheets as well as the crumpled and continuous areas. Fig. 1b shows the SEM image of 3D Sn/PPy composite. Because of the addition of Sn nanoparticles, the individual sheets show a more upstanding structure, and the edge of each sheet shows granuliform morphology. Sn nanoparticles can hardly be detected on the surface of PPy nanosheets, implying that almost all the Sn nanoparticles are contained inside the PPy layers. The low magnification SEM image clearly demonstrates the nanosheets network (Fig. 1c). Further investigation of the as-prepared sample by EDS mapping (Fig. 1d) confirms that Sn nanoparticles are highly dispersed in the PPy nanosheets. Besides tin and carbon, phosphorus and nitrogen are also detected, being consistent with the constituent of the 3D Sn/PPy composite.

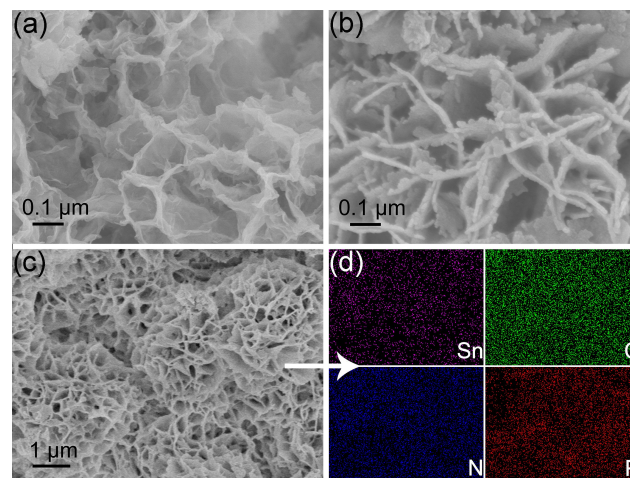


Fig. 1 SEM images of (a) 3D pure PPy network and (b-c) 3D Sn/PPy composite network. (d) Elemental mapping of 3D Sn/PPy composite showing the existence and highly dispersion of Sn.

To provide further insights into the morphology and structure of the resulting Sn/PPy nanosheets, TEM investigations are carried out. The well dispersed Sn nanoparticles (black dots) with uniform particle sizes of ~5 nm embedded in PPy nanosheets network (gray matrix) are clearly shown in Fig. 2a-c. The densely loading and low aggregation of Sn nanoparticles indicates that PPy nanosheets play an essential role in achieving good dispersion of the Sn nanoparticles. The corresponding HR-TEM image taken near the edge shows lattice fringes of Sn nanoparticles embedded in PPy nanosheets (Fig. 2d). A lattice spacing of 0.208 nm is recognized and can be ascribed to the (220) planes of tetragonal Sn as indicated by the red arrow in the inserted image of magnified lattice fringes. As we know, the small size of Sn nanoparticles is very

important to produce an optimal battery system as it can limit the absolute volume change of each Sn nanoparticle, and prevent pulverization or detachment from the current collector during cycling. This is beneficial for preserving electrical contact with the current collector and the integrity of the anode material. Furthermore, in Fig. 2d, a light dark amorphous layer (about 3-4 nm) outside the Sn nanoparticles is observed, confirming a vertical thickening of PPy layer due to the existence of Sn nanoparticles. This further demonstrates that the Sn nanoparticles are well embedded within the thin amorphous PPy layer rather than exposed on the outer surface. So the wrapping effect of PPy nanosheets can potentially help improve the structural and interfacial stabilization of Sn nanoparticles during cycling. What's more, the ultrathin *in-situ* coating layer can tightly link Sn nanoparticles with the conductive PPy network through chemical crosslinking, thus guaranteeing a continuous electrical connection for the interior active materials. For comparison, the SEM and TEM images of the Sn@PPy composite are shown in Fig. S2. Though a similar weight ratio of the Sn to PPy is used, no 3D network structure exists but granulated morphology with core/shell nanostructures. The TEM image (Fig. S2b) clearly demonstrates that a compact PPy coating layer is formed outside Sn nanoparticles through *in-situ* chemical oxidation polymerization. However, the Sn@PPy nanoparticles are agglomerated to form a larger unit through the binding effect of PPy. Besides, the thickness of the formed coating layer is about 20 nm, which is much thicker than that in 3D Sn/PPy composite.

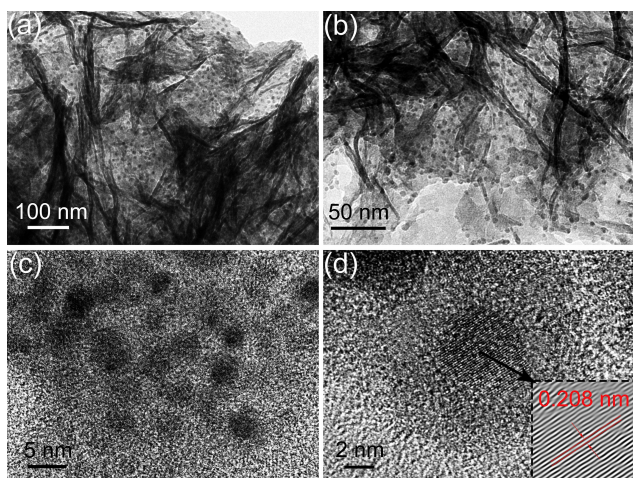


Fig. 2 (a-c) TEM and (d) HR-TEM images of Sn nanoparticles highly dispersed and embedded in PPy nanosheets.

The N_2 adsorption-desorption analysis reveals that the 3D Sn/PPy composite possesses a large BET specific surface area of $138.2 \text{ m}^2 \text{ g}^{-1}$ (Fig. 3), much higher than that of the Sn@PPy composite ($20.3 \text{ m}^2 \text{ g}^{-1}$). It confirms that the PPy nanosheets network provides a large contact surface for individual dispersion of well-adhered Sn nanoparticles so that more active materials can be loaded on to the current collector. Moreover, benefiting from the nanogaps formed between each neighboring nanosheet as well as large surface exposure, fast Li^+

intercalation into the inner layers of the active materials will be facilitated. As will be discussed later, the bespoke structure of the as-prepared 3D Sn/PPy composite that combines the 3D conductive network and flexible confining structure with ultrafine Sn nanoparticles is expected to contribute to an upgraded cycling performance of anode materials, especially high-rate performance.

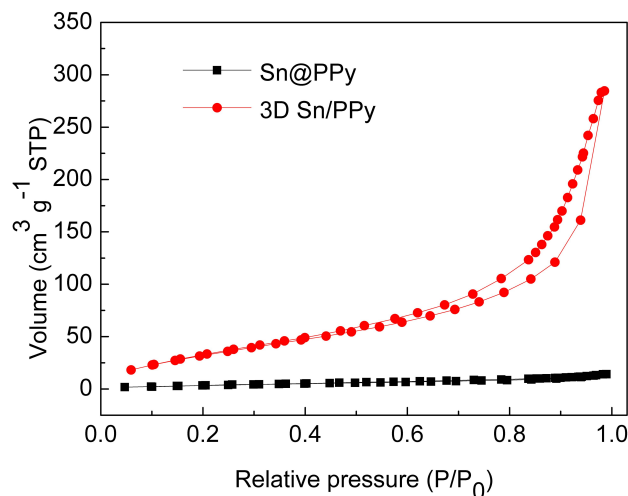


Fig. 3 Surface areas of 3D Sn/PPy composite and Sn@PPy composite.

Typical XRD patterns of the as-prepared Sn nanoparticles, pure 3D PPy, and 3D Sn/PPy composite are distinctly demonstrated in Fig. 4. Peaks at 30.6° , 32.0° , 43.9° , 44.9° , 55.3° , 62.5° , 63.8° , 64.6° , 72.4° , 73.2° and 79.5° are attributed to the Sn of the space group $I41/amd$ with a tetragonal structure of the space group $I41/amd$ with a tetragonal structure (JCPDS 04-0673). The broad peaks of Sn with low intensities indicate the existence of nanoscale Sn nanoparticles. Peaks at 25° observed in the pure PPy and 3D Sn/PPy composite correspond to periodicity paralleling to the polymer chains which implies the relative ordering structure of PPy. The existence of PPy can be further supported by the Raman spectrum (Fig. S3), in which bare PPy shows characteristic Raman peaks at 1361 and 1551 cm^{-1} , weak peaks at 988 , 938 , and 1252 cm^{-1} , which are assigned to C=C backbone stretching and ring-in plane deformation of PPy, indicating the successful polymerization of PPy [28]. The Sn/PPy composite shows both the peaks of Sn and PPy, though the intensity of the Sn peak is very weak relative to PPy. Since Raman spectroscopy is a surface-sensitive technique, this observation indicates that the surface of the Sn nanoparticles have been covered by PPy, which is consistent with the HR-TEM images of the composites. The mass loading of active Sn material is determined by the TGA results as shown in Fig. 5. In this temperature interval, the mass of PPy begins to decrease around 300°C because of the decomposition in the air under high temperature, and the decomposition is completed at $\sim 600^\circ \text{C}$ with a mass decreased to almost zero. Because the weight change of metal is small and can be neglected, the mass loss in the 3D Sn/PPy composite can

be attributed to the decomposition of PPy. Thus corresponding to the mass retention of the 3D Sn/PPy composite in the temperature region of 50-800 °C, the content of Sn in the composite is ca. 72 wt.%. Thus the Sn mass loading of each electrode is typically calculated to be around 0.45 mg cm⁻². It should be noted that this value has reached the level for practical battery application, and the mass loading can be potentially increased by adding more active Sn nanoparticles attached onto the PPy nanosheets network.

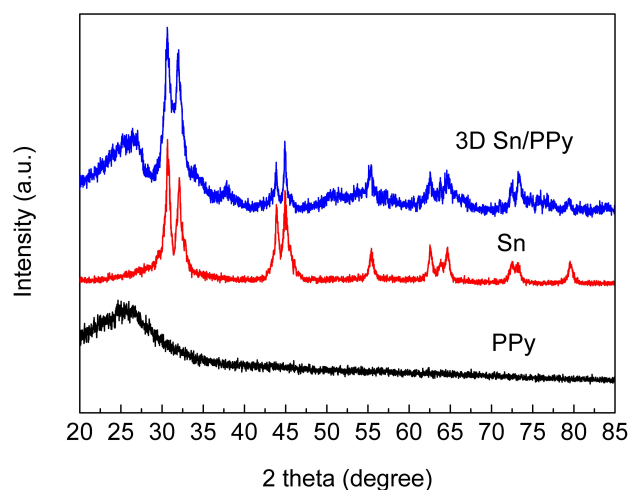


Fig. 4 XRD profiles of PPy, Sn nanoparticles, and 3D Sn/PPy composite.

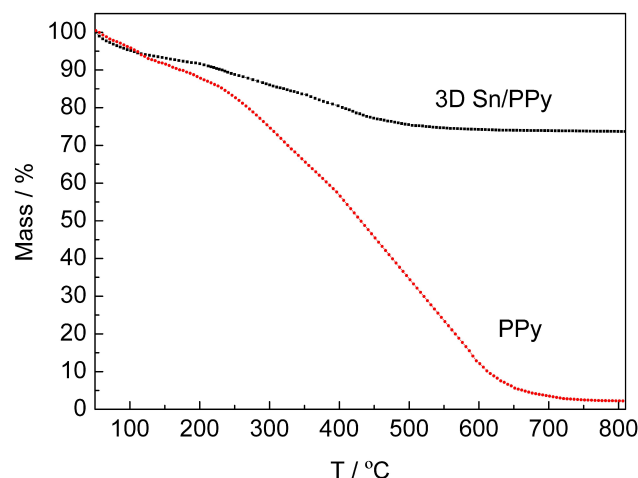


Fig. 5 TGA plots of 3D Sn/PPy composite and pure Sn nanoparticles obtained from 50 to 800 °C at a heating rate of 10 °C min⁻¹ in air.

A schematic depiction for the synthesis of the 3D Sn/PPy composite is presented in Fig. 6. The distinctive 3D PPy nanosheets network is obtained through an organic crystal surface-induced polymerization method in an aqueous suspension containing hydrated surfactant crystals of sodium dodecyl sulfate (SDS). Ionic hydrocarbon surfactant SDS can exist in the state of hydrated crystals when the temperature of the micelle solution drops to 0 °C [29]. The SDS hydrated

surfactant crystals act as a soluble template, showing a possible lamellar structure formed by SDS molecules. The growth of this PPy nanosheet arises from the hydrated crystal surface through a shape-copying process. The electrostatic interactions between growing cationic PPy chains and anionic surfaces of organic crystals during the polymerization drive the PPy replication of the hydrated crystal templates. Simultaneously, part of SDS molecules cover on the Sn nanoparticles with their hydrophobic sides, and their anionic hydrophilic groups facilitate the formation of ultrathin *in-situ* polymer coating outside Sn nanoparticles. It is anticipated that this method to prepare organic-inorganic composites will be very suitable for other metal materials. In the end, the SDS hydrated surfactant crystals can be removed by dissolving in DI water. Moreover, before adding APS, phytic acid is mixed into the solution as the conductive crosslinker and dopant to directly form a conducting polymer network free of insulating polymers [30]. Phytic acid reacts with PPy by protonating the imine groups on PPy, and each phytic acid molecule can interact with more than one PPy chain, this crosslinking effect not only results in the formation of connected PPy nanosheets network fixed with *in-situ* coated Sn nanoparticles, but also further improved the conductivity of the PPy nanosheets network through protonic acid doping [30]. In the end, the 3D Sn/PPy composite can be bladed onto a copper foil to form an electrode (see details in experiment parts).

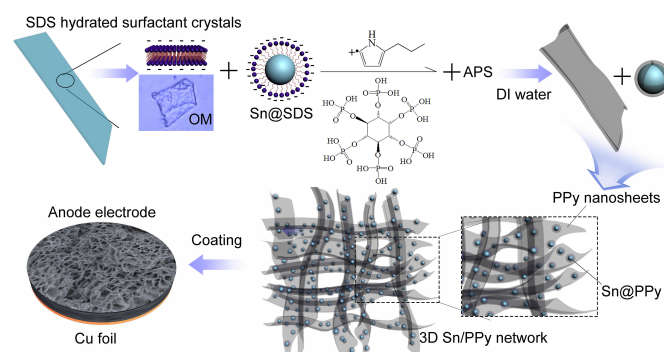


Fig. 6 Schematic illustration for the formation of the distinctive 3D PPy nanosheets network with ultrafine Sn nanoparticles embedded inside.

The unique morphology and structure of the as-prepared 3D Sn/PPy composite motivate us to further investigate its electrode performance. CV measurements are performed on coin cells at a scan rate of 0.1 mV s⁻¹ in the potential window of 0.01-3.0 V versus Li⁺/Li (Fig. 7). The CV profile of the 3D Sn/PPy composite electrode exhibits similar electrochemical characteristics as that of pristine Sn nanoparticles [31], indicating the PPy coating does not introduce changes to the electrochemical nature of active materials in this voltage range. During the first cathodic sweep, the broad reduction peak around 1.5 V is ascribed to the decomposition of the electrolyte to form solid-electrolyte interphase SEI film. Three small reduction peaks at 0.2, 0.37, and 0.57 V are assigned to the lithium insertion into Sn to form a Li_xSn alloy. Oxidation peaks

at 0.49, 0.61, and 0.8 V correspond to the delithiation reaction of Li_xSn alloy. All peaks are reproducible and stable after the first cycle, implying a good cycling stability of the Sn/PPy composite. In addition, in the following cycles, the reduction peaks shift to higher potentials while the oxidation peaks shift to lower potentials, indicating a lower charge-discharge polarization and an improvement of the reaction kinetics. This can be ascribed to the partly doping of PPy by LiPF_6 in the first few cycles, which to some extent enhances the electrical conductivity of PPy [32]. Meanwhile, the CV profile of pure 3D PPy electrode (0.01–3.0 V versus Li/Li^+) tested under the same condition shows its current density is about three orders of magnitude lower than that of the 3D Sn/PPy composite electrode, indicating negligible contribution from PPy to the capacity of the whole electrode.

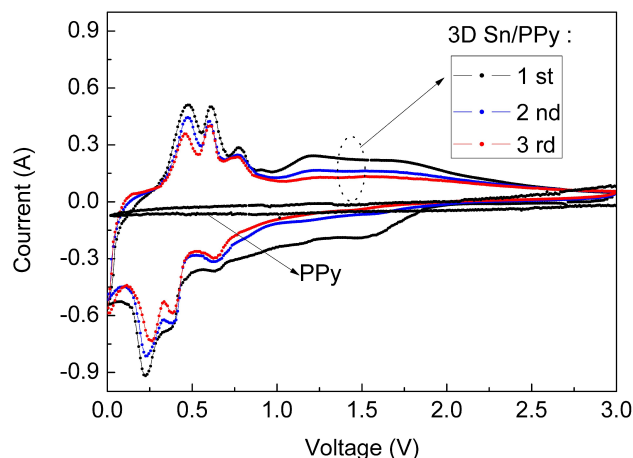


Fig. 7 CV measurements of the 3D Sn/PPy electrode for the first 3 cycles and pure PPy at a scan rate of 0.1 mV s^{-1} in the voltage range of 0.0–3.0 V (versus Li/Li^+).

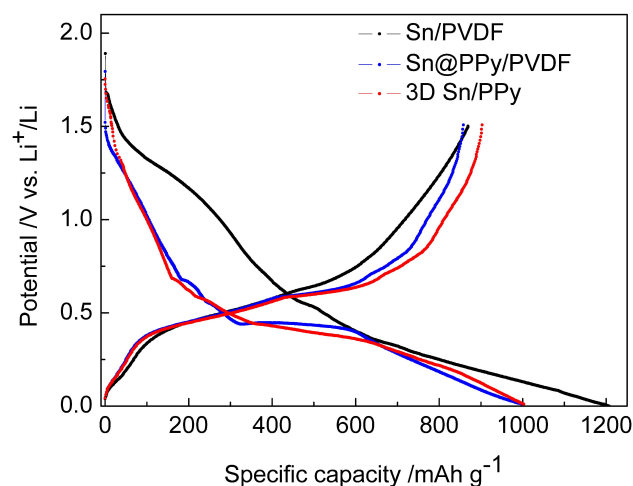


Fig. 8 Comparison of the potential profiles of the 3D Sn/PPy electrode, Sn@PPy/PVDF electrode and Sn/PVDF electrode in the first cycles.

The electrochemical cycling performance of the composite electrode is evaluated using galvanostatic charge/discharge

cycling from 1.5 to 0.01 V as shown in Fig. 8 and 9. Because pure PPy has no electrochemical active in this voltage range [33], all the specific capacities are calculated based on the weight of Sn nanoparticles which takes up about 72% mass fraction of the whole electrode. To further highlight the superiority of the 3D Sn/PPy composite as anode materials of lithium-ion batteries, the Sn@PPy/PVDF and Sn/PVDF electrodes are also investigated under the same conditions. Fig. 8 shows the voltage profiles of the three electrodes for the first cycle. The plateaus of them are similar except the voltage platform above 0.7 V in the first discharge curve which corresponds to the formation of SEI films. That platform of Sn/PVDF is evidently larger than that of the Sn@PPy/PVDF and 3D Sn/PPy electrodes. The initial lithiation of 3D Sn/PPy delivers a capacity of 1003 mAh g^{-1} and 89% of the inserted Li can be reversibly delithiated; and the Sn@PPy/PVDF delivers a discharge capacity of 998 mAh g^{-1} with a coulomb efficiency of 86%. While for Sn/PVDF electrode, the first discharge capacity is about 1073 mAh g^{-1} with a reversible capacity of 869 mAh g^{-1} . The capacity loss of the former two electrodes in the first cycle are smaller than that of the Sn/PVDF electrode, illustrating that the coating layer can effectively reduce the irreversible capacity in the initial cycles which is mainly attributed to the formation of SEI film. Furthermore, at a constant current density of 200 mA g^{-1} , the 3D Sn/PPy composite electrode exhibits a high reversible capacity of 766 mAh g^{-1} over 200 cycles, corresponding to 85% capacity retention (Fig. 9a). The slow shrinkage of the reversible capacities implies a high cycling stability of this electrode. The coulomb efficiency of the 3D Sn/PPy electrode in the first cycle is about 88.5% owing to the formation of SEI film which consumes a certain percentage of lithium (Fig. 9b), while the average coulomb efficiency from the 2nd to 200th cycle reaches to 99.8%. The relatively high and stable coulomb efficiency achieved by 3D Sn/PPy electrode indicates that the embedment of active Sn nanoparticles can largely avoid detrimental reactions between Sn and electrolyte, so that this anode material can remain the reversibility of its electrochemical reactions very well. For Sn@PPy/PVDF electrode with no 3D network structure, it is observed that the capacity fades drastically to a value of 375 mAh g^{-1} after 200 cycles, corresponding to only 44% capacity retention. Without enough active materials' exposure to allow effective Li^+ intercalation as in the 3D Sn/PPy electrode, it takes time for electrolyte ions to reach the inner layer of electrode material so the tortuous and elongated ion transport path lengths inevitably lead to impaired electrode kinetics and reduced capacity, or more seriously, only the surface of the active material involves in the electrochemical reaction. On the other hand, the Sn/PVDF electrode loses >70% of its initial capacity with an average coulomb efficiency of only 92.6% after 50 cycles. This is owing to the lack of cushion protection and the thickening of SEI film. It is therefore further confirmed that the coulomb efficiency can be improved by surface modification by ultrathin PPy coating. In this sharp contrast, the cycle stability and reversible capacity of 3D Sn/PPy electrode are markedly

superior to that of the Sn@PPy/PVDF electrode and Sn/PVDF electrode. Besides the reasons that have been mentioned above, this can also be attributed to efficient binding ability of the PPy network in maintaining good contacts and sufficient adhesion of the electrode material to the current collector. The replacement of insulating binder can effectively suppress sluggish kinetics caused by the broken electric connections during cycling. More importantly, the increased reactive sites of the high dispersion of ultrafine Sn nanoparticles provided by the PPy nanosheets network with large contact surface can effectively maximize the accessible capacity. Above all, the synergistic effect of the conductive 3D network matrix and PPy coating layer is the key issue to enhance the structural stability and cycle performance of Sn active materials. We note that an increase of the capacity is observed during the initial cycles in both electrodes, and for Sn@PPy/PVDF electrode, it is more serious (Fig. 9a). The origin of this activation step can be possibly attributed to the delayed wetting of electrolyte into the composite electrode.

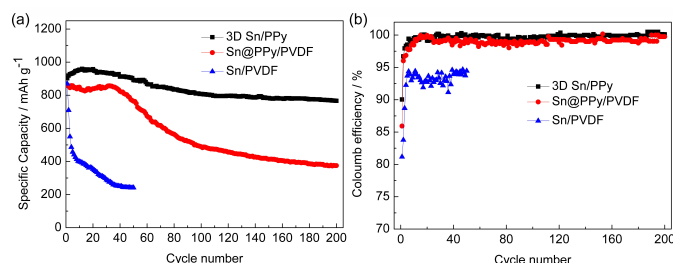


Fig. 9 (a) Electrochemical cycling performance and (b) coulomb efficiency of 3D Sn/PPy electrode, Sn@PPy/PVDF electrode, and Sn/PVDF electrode at a charge/discharge current of 200 mA g⁻¹.

Taking advantages of the unique 3D conductive network structure, the 3D Sn/PPy electrode also shows excellent rate capabilities at continuously variable current densities. Fig. 10a shows the charge/discharge curves of 3D Sn/PPy electrode at different current densities. The composite shows a relatively smooth voltage profile due to the increased surface area in nanoparticle electrodes compared with bulk materials. Because different surface and subsurface sites react at slightly different potentials, the increased surface-to-bulk ratios of Sn nanoparticles lead to a concomitant dispersion of values at which the electrochemical reaction takes place [31]. According to Fig. 10b, specific capacities are shown to decrease as the scan rate increases since increasing the scan rate provides less participation of the active material. Nevertheless, we can see that even at a high charge/discharge current of 2000 mA g⁻¹, the lithiation potential still shows a sloping profile between 1.5 and 0.01 V, approximately consistent with previously reported Li insertion to form Li_xSn [2]. What is more, as shown in Fig. 10b, reversible capacities of the 3D Sn/PPy composite electrode are 945, 904, 820, 713, and 610 mAh g⁻¹ at the increasing current densities of 0.1, 0.2, 0.5, 1, 2 A g⁻¹, respectively. When the current densities decrease back from 2 A g⁻¹ to 1, 0.5, 0.2, and 0.1 A g⁻¹, the reversible capacities of the 3D Sn/PPy recover

from 610 mAh g⁻¹ to 695, 750, 791, and 842 mAh g⁻¹. When the current density returns to the initial 0.1 A g⁻¹ after 180 cycles, the composite electrode retains its capacity of about 835 mAh g⁻¹. In the last 20 cycles at 200 mA g⁻¹, the capacity still retains about 756 mAh g⁻¹, while the capacities of the Sn@PPy/PVDF electrode decrease rapidly to a capacity of about 300 mAh g⁻¹ at a current density of 500 mA g⁻¹ after 60 cycles. The results can be closely ascribed to the incorporation of ultrathin *in-situ* coating and 3D PPy conductive network which can enhance the physical and electrical connections between Sn nanoparticles and the current collector, and provide a short path length for Li⁺ intercalation, thereby maximizing the effective electrochemical utilization of the active materials and ensuring a reversible lithium insertion/extraction process even at high current rates.

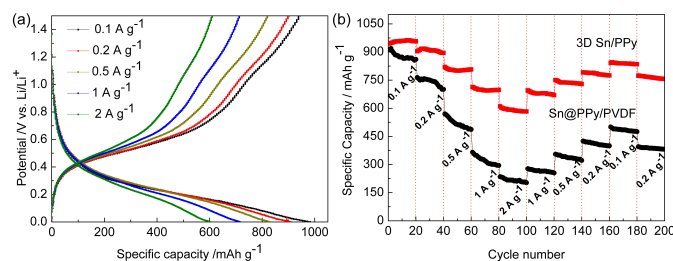


Fig. 10 (a) Charge/Discharge profiles of 3D Sn/PPy electrode at various current densities. (b) Rate performance demonstration of 3D Sn/PPy and Sn@PPy/PVDF electrodes at different current densities.

In fact, the high rate capability and the cycle stability are tightly related to the thickness of SEI film, interfacial charge-transfer process, and lithium-ion diffusion in the composite. To gain further insight into its electrochemical performance, electrochemical impedance spectroscopy (EIS) measurements are carried out at room temperature to verify the interfacial stabilization effect of thin PPy *in-situ* coating and conductivity-boosting effect of the conductive network. In order to highlight the effect of conductive PPy network, we also tested the control electrode Sn@PPy/PVDF. EIS results are collected on the cells at the fully delithiation state (Fig. 11a, b). The high frequency intercept at the real impedance (Z') axis is generally considered as electrical conductivity of electrodes, electrolyte, separator and electrical contacts (R_e). For 3D Sn/PPy electrode, the intercept is smaller than that of the Sn@PPy/PVDF electrode as magnified in the insert image in Fig. 11a. The PPy network functioning as conductive binder to some extent reduces the internal resistance of the electrode when compared with the traditional PVDF system. The first depressed semicircle in the high-frequency range is correlated to the Li⁺ migration resistance (R_{sf}) through the SEI film. The second semicircle in the medium-frequency range corresponds to the charge-transfer resistance (R_{ct}) between the surface films and the active material. We mainly focus on the comparison of $R_{(sf+ct)}$ here. As shown in Fig. 11a, after 3 cycles, the R_{sf} diameter of 3D Sn/PPy is similar to that of the Sn@PPy/PVDF according to the Nyquist plots, while the diameter of R_{ct} semicircle for 3D Sn/PPy is much smaller than that of the Sn@PPy/PVDF. The

result suggests that the 3D Sn/PPy electrode material possesses a much lower charge-transfer resistance and improved reaction kinetics, leading to its higher initial and cycle capacity. Meanwhile, the low-frequency tail is also different, which can be compared qualitatively with reference to the Li^+ transfer kinetics in the electrode materials [13]. The steeper low-frequency tail of 3D Sn/PPy electrode indicates higher lithium ion conductivity than that of the Sn@PPy/PVDF electrode. The improvement of lithium ion transport properties of 3D Sn/PPy electrode strongly depend on its 3D open structure and the ultrathin PPy coating layer since the thickness of the polymer layer also has a great influence on the facility for lithium ion transport [34]. So as expected, the designed 3D structure with ultrathin coating can improve the stability of SEI films, the rate of charge-transfer, and Li^+ kinetics for insertion/extraction, thus resulting in improved cycle performance and rate performance. For the 3D Sn/PPy composite electrode, the diameters of R_{ct} semicircles decrease for the first few cycles. This can be attributed to the slow wetting of electrolyte and the partly doping effect by LiPF_6 . During the lithiation/delithiation process, PPy can be *n*-doped/dedoped, thus aiding the electrochemical process of electrode materials [32]. In addition, no obvious impedance increase is detected after cycling for more than 100 times, indicating the formation of a stable SEI film and the efficient electronic/ionic transport during cycling.

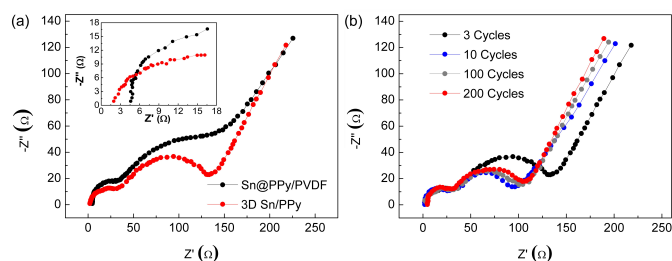


Fig. 11 (a) EIS spectra of the 3D Sn/PPy and Sn@PPy/PVDF electrodes after 3 cycles at the fully delithiation state. (b) EIS spectra of the 3D Sn/PPy electrode after 3, 10, 100 and 200 cycles at fully delithiation states.

Furthermore, the benefit of this bespoke structure relies in the electrode integrality in long-term operation. The well preserved structure of 3D Sn/PPy after the electrochemical cycling process is shown in Fig. 12a, b. It is a notable point that after 200 cycles, the nanosheets network is well preserved with slightly thickened PPy nanosheets, indicating the formation of a thin and stable SEI film owing to the conductive modification of the Sn surface by the *in-situ* polymerized PPy. What's more, TEM image (Fig. 12c, d) shows that after 200 electrochemical cycles, Sn nanoparticles are still confined inside the PPy nanosheets without losing electrical contact, and the Sn nanoparticles of ~ 5 nm did not further break or aggregate since they maintain their initial sizes and morphology after repeated charge-discharge cycles. This demonstrates the long-term stability of the 3D Sn/PPy anode material. By contrast, the structure of Sn@PPy/PVDF electrode is to some extent destroyed. As shown in Fig. S4a, though the Sn nanoparticles

are still coated in the conformal PPy layer, they are broken into smaller pieces during cycling. Besides, since the lack of open structure for facile Li^+ transport and electrolyte permeation, a thick SEI film is formed on the surface of Sn@PPy/PVDF electrode due to the concentrated lithiation/delithiation reactions of the surface active materials (Fig. S4b).

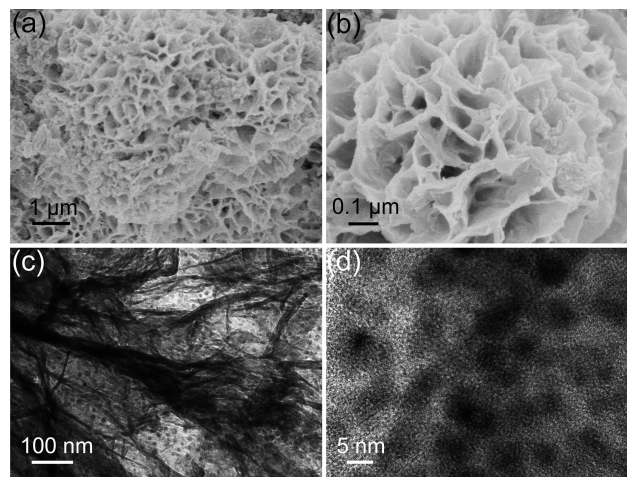


Fig. 12 (a, b) SEM and (c, d) TEM images of the 3D Sn/PPy nanosheets network electrode after 200 cycles at a charge/discharge current of 200 mA g^{-1} .

Generally, as illustrated in Fig. 13, for larger particles, they often suffer serious partial pulverization and cracking because of the large volume change and the stresses upon lithiation/delithiation [9]. The broken particles with newly formed active surfaces will induce the repeated formation of SEI film which causes consumption of abundant Li^+ and a large irreversible capacity. Besides, it's easy to cause broken electric connections and peeling off from the current collector due to the weakened contact, thus leading to fast decay in capacity upon cycling. In our work, the size of the Sn nanoparticles is very small so it can significantly reduce the strain generated during the lithiation/delithiation processes and then suppress the fracture of Sn nanoparticles. Meanwhile, on account of the homogeneous dispersion of Sn nanoparticles, the generated stress upon cycling would evenly distribute in the whole composite as well as the electrode, preventing local cracking. What's more, the wrapping effect of PPy nanosheets can potentially help better improve the structural and interfacial stabilization of Sn nanoparticles during cycling. To be specific, it can avoid the exfoliation and aggregation of Sn nanoparticles during cycling, and effectively prevent the direct contact between the active materials and electrolyte to form a stable solid electrolyte interphase (SEI) film [13]. Besides, it can offer stable and continuous electronic transmission pathways during repeated lithiation/delithiation processes. Notably, these results further certify that the advantages of ultrafine Sn nanoparticles and PPy nanosheets with ultrathin *in-situ* coating function can effectively avoid the widespread problems of pulverization and agglomeration of active anode materials, thus ensuring the long cycle stability.

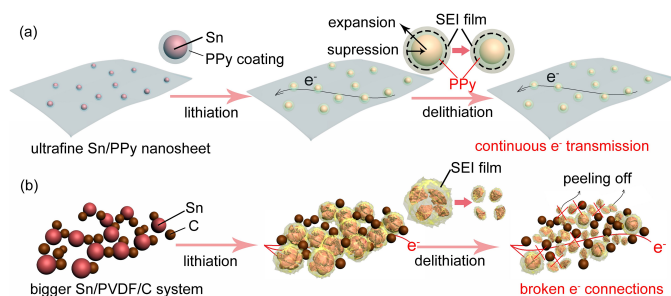


Fig. 13 Schematic illustration of the synergistic contributions of ultrafine Sn nanoparticles and the designed 3D PPy network to address the unstable problems existing in current electrode materials during repeated lithiation/delithiation processes: (a) 3D ultrafine Sn/PPy nanosheets network; (b) bigger Sn/PVDF/acetylene black system.

Conclusions

In conclusion, we have developed a facile and scalable solution process to fabricate high-performance binder-free lithium-ion battery anode material composed of 3D flexible PPy nanosheets network anchored with ultrafine Sn nanoparticles. The greatly improved cycling performance, rate capability and life-span of the electrode arises from the desirable feature of the well engineered 3D Sn/PPy composite, such as lessened internal strain of the electrode, shortened pathway length for ion transport, and maximized accessible capacity. By combining fascinating advantages of ultrafine Sn nanoparticles and 3D conductive PPy nanosheets network matrix, this multifunctional composite is a promising anode material for highly efficient lithium-ion batteries. Optimistically, this type of multifunctional composite structure can be extended for the fabrication of other cathode and anode electrode materials to achieve higher performance, and this solution synthesis and electrode fabrication processes are highly scalable and compatible in the battery manufacturing technology.

Acknowledgements

This work was financially supported by the National Natural Science Foundation of China (No.51143009 and 51273145).

Notes and references

^a School of Materials Science and Engineering, Tianjin University, Tianjin 300072, P.R. China.

^b Tianjin Key Laboratory of Composite and Functional Materials, Tianjin 300072, P.R. China.

* Corresponding author. Tel: +86-22-27406127; fax: +86-22-27406127. Email address: xhxu_tju@eyou.com.

- 1 M. Armand, J. M. Tarascon, *Nature*, 2008, **451**, 652.
- 2 M. Winter, J. O. Besenhard, *Electrochim. Acta*, 1999, **45**, 31.
- 3 K. T. Lee, Y. S. Jung, S. M. Oh, *J. Am. Chem. Soc.*, 2003, **125**, 5652.
- 4 Y. H. Xu, J. C. Guo, C. S. Wang, *J. Mater. Chem.*, 2012, **22**, 9562.
- 5 D. Deng, J. Y. Lee, *Angew. Chem. Int. Ed.*, 2009, **48**, 1660.
- 6 D. N. Wang, X. F. Li, J. L. Yang, J. J. Wang, D. S. Geng, R. Y. Li, M. Cai, T. K. Sham, X. L. Sun, *Phys. Chem. Chem. Phys.*, 2013, **15**, 3535.

- 7 S. Q. Chen, P. Chen, M. H. Wu, D. Y. Pan, Y. Wang, *Electrochem. Commun.*, 2010, **12**, 1302.
- 8 Y. H. Xu, Q. Liu, Y. J. Zhu, Y. H. Liu, A. Langrock, M. R. Zachariah, C. S. Wang, *Nano Lett.*, 2013, **13**, 470.
- 9 Z. Q. Zhu, S. W. Wang, J. Du, Q. Jin, T. R. Zhang, F. Y. Cheng, J. Chen, *Nano Lett.*, 2014, **14**, 153.
- 10 Z. F. Li, H. Y. Zhang, Q. Liu, Y. D. Liu, L. Stanciu, J. Xie, *ACS Appl. Mater. Interfaces*, 2014, **6**, 5996.
- 11 J. J. Cai, P. J. Zuo, X. Q. Cheng, Y. H. Xu, G. P. Yin, *Electrochem. Commun.*, 2010, **12**, 1572.
- 12 D. L. Ma, Z. Y. Cao, H. G. Wang, X. L. Huang, L. M. Wang, X. B. Zhang, *Energ. Environ. Sci.*, 2012, **5**, 8538.
- 13 F. Han, D. Li, W. C. Li, C. Lei, Q. Sun, A. H. Lu, *Adv. Funct. Mater.*, 2013, **23**, 1692.
- 14 H. J. Ding, B. Yao, J. K. Feng, J. X. Zhang, *J. Mater. Chem. A*, 2013, **1**, 11200.
- 15 S. Y. Chew, Z. P. Guo, J. Z. Wang, J. Chen, P. Munroe, S. H. Ng, L. Zhao, H. K. Liu, *Electrochem. Commun.*, 2007, **9**, 941.
- 16 P. J. Zhang, L. B. Wang, J. Xie, L. W. Su, C. A. Ma, *J. Mater. Chem. A*, 2014, **2**, 3776.
- 17 H. W. G. H. Yu, L. J. Pan, N. Liu, M. T. McDowell, Z. N. Bao, Y. Cui, *Nat. Commun.*, 2013, **4**, 1943.
- 18 Z. G. Yin, Y. H. Ding, Q. D. Zheng, L. H. Guan, *Electrochem. Commun.*, 2012, **20**, 40.
- 19 M. Sindoro, Y. H. Feng, S. X. Xing, H. Li, J. Xu, H. L. Hu, C. C. Liu, Y. W. Wang, H. Zhang, Z. X. Shen, H. Y. Chen, *Angew. Chem. Int. Ed.*, 2011, **50**, 9898.
- 20 J. X. Zhu, D. Yang, X. H. Rui, D. Sim, H. Yu, H. H. Hng, H. E. Hoster, P. M. Ajayan, Q. Y. Yan, *Small*, 2013, **9**, 3390.
- 21 M. Tian, W. Wang, Y. J. Wei, R. G. Yang, *J. Power Sources*, 2012, **211**, 46.
- 22 G. Ferrara, C. Arbizzani, L. Damen, M. Guidotti, M. Lazzari, F. G. Vergottini, R. Inguanta, S. Piazza, C. Sunseri, M. Mastragostino, *J. Power Sources*, 2012, **211**, 103.
- 23 C. Zhou, Y. W. Zhang, Y. Y. Li, J. P. Liu, *Nano Lett.*, 2013, **13**, 2078.
- 24 J. Qu, H. Q. Li, J. J. Henry, S. K. Martha, N. J. Dudney, H. B. Xu, M. F. Chi, M. J. Lance, S. M. Mahurin, T. M. Besmann, S. Dai, *J. Power Sources*, 2012, **198**, 312.
- 25 T. Jiang, S. C. Zhang, X. P. Qiu, W. T. Zhu, L. Q. Chen, *J. Power Sources*, 2007, **166**, 503.
- 26 C. Guan, X. L. Li, Z. L. Wang, X. H. Cao, C. Soci, H. Zhang, H. J. Fan, *Adv. Mater.*, 2012, **24**, 4186.
- 27 X. Fan, X. N. Tang, D. Q. Ma, P. B., A. N. Jiang, J. Zhu, X. H. Xu, *J. Solid State Electrochem*, 2014, **18**, 1137.
- 28 H. N. T. Le, M. C. Bernard, B. Garcia-Renaud, C. Deslouis, *Synth. Met.*, 2004, **140**, 287.
- 29 S. S. Jeon, J. K. Park, C. S. Yoon, S. S. Im, *Langmuir*, 2009, **25**, 11420.
- 30 L. J. Pan, G. H. Yu, D. Y. Zhai, H. R. Lee, W. T. Zhao, N. Liu, H. L. Wang, B. C. K. Tee, Y. Shi, Y. Cui, Z. N. Bao, *PNAS*, 2012, **109**, 9287.
- 31 L. P. Xu, C. J. Kim, A. K. Shukla, A. G. Dong, T. M. Mattox, D. J. Milliron, J. Cabana, *Nano Lett.*, 2013, **13**, 1800.
- 32 Z. J. Du, S. C. Zhang, Y. Liu, J. F. Zhao, R. X. Lin, T. Jiang, *J. Mater. Chem.*, 2012, **22**, 11636.
- 33 K. S. Ryu, B. M. Moon, J. Joo, S. H. Chang, *Polymer*, 2001, **42**, 9355.
- 34 P. M. Dzewonski, M. Grzeszczuk, *Electrochim. Acta*, 2010, **55**, 3336.